The Astrophysical Journal, 974:47 (13pp), 2024 October 10 https://doi.org/10.3847/1538-4357/ad6561

Plasma Dynamics and Nonthermal Particle Acceleration in 3D Nonrelativistic Magnetic Reconnection

Qile Zhang[1], Fan Guo[1], William Daughton[1], Xiaocan Li[2], and Hui Li[1]
[1] Los Alamos National Laboratory, Los Alamos, NM 87545, USA; qlzhanggo@gmail.com, guofan@lanl.gov, daughton@lanl.gov, hli@lanl.gov
[2] Dartmouth College, Hanover, NH 03755, USA; phyxiaolee@gmail.com
Received 2024 March 19; revised 2024 July 12; accepted 2024 July 17; published 2024 October 3

Abstract

Understanding plasma dynamics and nonthermal particle acceleration in 3D magnetic reconnection has been a long-standing challenge. In this paper, we explore these problems by performing large-scale fully kinetic simulations of multi-X-line plasmoid reconnection with various parameters in both the weak- and strong-guide-field regimes. In each regime, we have identified its unique 3D dynamics that lead to field-line chaos and efficient acceleration, and we have achieved nonthermal acceleration of both electrons and protons into power-law spectra. The spectral indices agree well with a simple Fermi acceleration theory that includes guide-field dependence. In the low-guide-field regime, the flux rope kink instability governs the 3D dynamics for efficient acceleration. The weak dependence of the spectra on the ion-to-electron mass ratio and β ($\ll 1$) implies that the particles are sufficiently magnetized for Fermi acceleration in our simulations. While both electrons and protons are injected at reconnection exhausts, protons are primarily injected by perpendicular electric fields through Fermi reflections and electrons are injected by a combination of perpendicular and parallel electric fields. The magnetic power spectra agree with in situ magnetotail observations, and the spectral index may reflect a reconnection-driven size distribution of plasmoids instead of the Goldreich–Sridhar vortex cascade. As the guide field becomes stronger, the oblique flux ropes of large sizes capture the main 3D dynamics for efficient acceleration. Intriguingly, the oblique flux ropes can also experience flux rope kink instability, to drive extra 3D dynamics. This work has broad implications for 3D reconnection dynamics and particle acceleration in heliophysics and astrophysics.

Unified Astronomy Thesaurus concepts: Solar magnetic reconnection (1504); Interplanetary particle acceleration (826); Space plasmas (1544); Plasma astrophysics (1261)

1. Introduction

Magnetic reconnection is a fundamental physics process in magnetized plasmas that releases magnetic energy and drives particle acceleration in various energetic phenomena in space and astrophysics (Yamada et al. 2010). Energetic particles are often observed during magnetic reconnection in space and in solar plasmas with low plasma β—for example, in Earth's magnetotail (Ergun et al. 2020; Oka et al. 2023), the heliospheric current sheet (Desai et al. 2022; Zhang et al. 2024), coronal interchange reconnection (Bale et al. 2023), and solar flares (Gary et al. 2018; Chen et al. 2020). Magnetic reconnection is observed to accelerate electrons (Krucker et al. 2010; Lin 2011; Oka et al. 2015, 2018; Gary et al. 2018), protons (Omodei et al. 2018; Cohen et al. 2020; Bale et al. 2023), and heavier ions (Cohen et al. 2020; Desai et al. 2022; Bale et al. 2023) into nonthermal power-law energy distributions $f \propto E^{-p}$ (with a wide range of spectral indices p ranging from 3 to 9). The nonthermal acceleration often occurs simultaneously for ions and electrons (Shih et al. 2009; Ergun et al. 2018, 2020). This indicates a common acceleration process in low-β reconnection for both ions and electrons. However, the underlying mechanisms have been challenging to understand, since most previous studies have failed to produce the simultaneous ion and electron power laws in self-consistent kinetic reconnection simulations (Dahlin et al. 2014, 2017; Li et al. 2017, 2018, 2019b, 2021; Guo et al. 2020). Meanwhile, during acceleration, reconnection also drives a turbulent state, as seen in the magnetotail (Ergun et al. 2018, 2020) and solar flares (Cheng et al. 2018; French et al. 2019). Unfortunately, the relation between reconnection and turbulence is also unclear.

Recent studies have found the major acceleration mechanism to be the Fermi acceleration mechanism (Drake et al. 2006; Dahlin et al. 2014, 2016, 2017; Guo et al. 2014; Li et al. 2017, 2018, 2019b), where particles bounce back and forth off contracting field lines to reach high energy. Since the Fermi acceleration rate is proportional to the particle energy, at high energy it will overrun the acceleration by the parallel electric field (Le et al. 2009; Haggerty et al. 2015; Dahlin et al. 2016; Zhang et al. 2019a, 2019b). Since the Fermi mechanism is driven by field-line curvature, and the curvature is strongest in the low-guide-field regime, this mechanism is most efficient with a low guide field (Dahlin et al. 2016; Li et al. 2017, 2018, 2019b; Arnold et al. 2021). The energy gain is strongest in the weak-guide-field regime and weaker for higher guide fields. However, magnetic islands in 2D can trap energetic electrons to prevent further Fermi acceleration (Dahlin et al. 2014; Li et al. 2017; Johnson et al. 2022). Previous studies show that 3D turbulent dynamics that produce field-line chaos can facilitate electron transport out of magnetic islands toward acceleration regions (reconnection exhausts) for more efficient Fermi acceleration (Dahlin et al. 2017; Li et al. 2019b). This stronger acceleration in 3D can help to form sustainable power laws for electrons (Li et al. 2019b). However, it is still not clear how ions and electrons can be both accelerated and develop power-law energy spectra, as observations have indicated, and what

are the origin and nature of the turbulent state in the reconnection region, as will be further discussed below.

Recently, Zhang et al. (2021) for the first time produced simultaneous ion and electron power laws in fully kinetic 3D simulations in the low-guide-field regime ($b_g < 0.5$). They achieved these power laws by taking advantage of the domain size threshold for the flux rope kink instability (of the tearing-mode-generated magnetic flux ropes; Dahlburg et al. 1992; Zhang et al. 2021) in the 3D domain design. This instability can disrupt and fragmentize the flux ropes (see also Zhang et al. 2024), to turn the reconnection layer into a turbulent state. This controls the 3D field-line chaos that facilitates efficient Fermi acceleration. Note that this instability is distinct from the more recognized drift-kink instability (Daughton 1998; Zenitani & Hoshino 2005; Liu et al. 2011), where the current sheet flaps. This study (Zhang et al. 2021) creates new opportunities to study 3D reconnection dynamics, as well as ion and electron acceleration in fully kinetic 3D simulations. In this paper, we use these simulations to further explore important aspects, such as 3D dynamics, parameter dependence, injection physics, and magnetic power spectra.

While the Fermi acceleration is most efficient in the low-guide-field regime, it is still important in the regime with a somewhat higher guide field ($0.5 < b_g \lesssim 1$). The ion and electron acceleration with such guide fields also commonly occurs in the solar corona, solar flares, solar wind, and the magnetosphere. Thus, it is important to achieve and understand the nonthermal ion and electron acceleration in this regime. Previous studies have suggested that the 3D turbulence and field-line chaos that facilitate efficient acceleration are driven by the overlapping oblique tearing-mode flux ropes (Onofri et al. 2006; Bowers & Li 2007; Daughton et al. 2011; Liu et al. 2013). However, the tearing modes from kinetic reconnection current sheets are at kinetic scales, which are usually much smaller than the system size. While earlier studies have recognized their chaotic and turbulent nature (Daughton et al. 2011; Liu et al. 2013; Dahlin et al. 2017), it is not completely clear what happens after these kinetic-size flux ropes continue to grow as reconnection proceeds. Moreover, in light of the flux rope kink instability for low guide fields, the oblique flux ropes could also be subject to the kink instability. It is thus unclear whether the overlapping oblique flux ropes are the only important process in the 3D turbulent dynamics with a guide field. Therefore, in this paper, we will explore the higher-guide-field regime regarding the 3D dynamics and nonthermal acceleration for ions and electrons.

This paper is arranged as follows. In Section 3, after we demonstrate nonthermal ion and electron acceleration in the low-guide-field regime using 3D fully kinetic particle-in-cell (PIC) simulations, we explore additional important aspects, such as plasma β and the ion-to-electron mass ratio dependence, injection process, and magnetic power spectra, to gain further insight into the acceleration process. We find that the magnetic power spectra agree well with in situ magnetotail observations, and the spectral indices may reflect a reconnection-driven size distribution of magnetic flux ropes (or islands) instead of the Goldreich–Sridhar vortex cascade. Then, in Section 4, we switch to the higher-guide-field regime. We find in our simulations that the initially small flux ropes from oblique tearing modes can keep on growing while maintaining their oblique angles and advecting with the large bidirectional reconnection outflows—eventually becoming large and proportional to the system size. It is the flux ropes of large sizes (proportional to the system size) that control the domain size threshold to capture the 3D field-line chaos for efficient acceleration. By taking advantage of this threshold, for the first time, our 3D PIC simulations with higher guide fields accelerate both ions and electrons into power-law energy spectra. The power-law indices are consistent with the Fermi acceleration predictions, with steeper spectral slopes than the low-guide-field regime due to the weaker acceleration. We discover that the oblique flux ropes can also be kink-unstable—which gives rise to another new domain size threshold—driving extra 3D dynamics to the reconnection layer. However, this oblique flux rope kink instability (and its driven 3D dynamics) does not appear to substantially further enhance the acceleration for ions and electrons in our simulations, with ions somewhat more enhanced than electrons. These results have broad applications for particle acceleration by reconnection in the magnetosphere, solar wind, and solar corona.

2. Simulation Setup

We use the VPIC code that solves the Vlasov–Maxwell equations (Bowers et al. 2008). The 3D simulations start from a force-free layer $\boldsymbol{B} = B_0 \tanh(z/\lambda)\boldsymbol{e_x} + \sqrt{B_0^2\,\mathrm{sech}^2(z/\lambda) + B_g^2}\,\boldsymbol{e_y}$, with a uniform plasma density $n_i = n_e = n_0$. B_0 is the reconnecting field, B_g is the guide field, and λ is the half-thickness of the layer, which is set to be one ion inertial length d_i. Electrons carry the initial current that satisfies Ampère's law. The ratio of the plasma frequency to electron cyclotron frequency ω_{pe}/Ω_{ce} is set to be 1. The default grid size is $\Delta x = \Delta y = \Delta z = 0.0488 d_i$ (which changes in some simulations, as shown in Table 1), with 150 particles per cell for each species. Boundary conditions are periodic in x and y, and conducting for fields and reflecting for particles in z. A small long-wavelength perturbation with $B_z = 0.02B_0$ is included to initiate reconnection. To limit the influence of periodic boundaries, unless specified, all simulations terminate at about 1.3 Alfvén crossing time L_x/V_A before the acceleration stagnates. A set of simulations has been conducted to study the underlying processes for different guide fields (from 0.2 to 1); electron/proton β, based on reconnecting fields that store available magnetic energy (from 0.02 to 0.08); domain sizes ($L_x = 75 - 300 d_i$); and the mass ratio ($m_i/m_e = 25$ or 100 with corresponding $c/V_A = 5$, 10). These simulations are summarized in Table 1. The "field-line chaos" column in Table 1 indicates whether the simulations show 3D effects with chaotic field lines.

3. Reconnection with a Low Guide Field

3.1. 3D Dynamics

In the low-guide-field regime, we find that the $m = 1$ flux rope kink instability drives the turbulent 3D dynamics by disrupting the flux ropes (Zhang et al. 2021). This belongs to the "external kink instability" in plasma physics. The flux ropes only become $m = 1$ kink-unstable when their length is long enough to make the safety factor at the edge of the flux ropes

$$q_{\mathrm{edge}} \sim \pi b_g D/L_y < 1 \tag{1}$$

(Oz et al. 2011; the "Kruskal–Shafranov limit"), where D is the typical diameter of the flux ropes. This means that the instability of flux ropes takes place when L_y exceeds a

Table 1
Simulations Discussed in This Paper

Run	L_x/d_i	L_y/d_i	L_z/d_i	$\Delta x/d_i$	β_{xe}	B_g/B_0	m_i/m_e	3D Field-line Chaos
1	150	6.25	62.5	0.0488	0.02	0.2	25	No
2	150	12.5	62.5	0.0488	0.02	0.2	25	Yes
3	300	25.0	125.0	0.0488	0.02	0.2	25	Yes
4	150	12.5	62.5	0.0488	0.08	0.2	25	Yes
5	75	6.25	31.25	0.0488	0.02	0.2	25	Yes
6	75	6.25	31.25	0.0244	0.02	0.2	100	Yes
7	150	15.625	62.5	0.0488	0.02	0.6	25	Yes
8	150	6.25	62.5	0.0488	0.02	0.6	25	No
9	150	25	62.5	0.0488	0.02	0.6	25	Yes
10	150	75	62.5	0.0488	0.02	0.6	25	Yes
11	300	50.0	125.0	0.061	0.03125	0.6	25	Yes
12	300	50.0	125.0	0.061	0.03125	1.0	25	Yes

Note. β_{xe} means electron β, based on reconnecting fields. The the last column "3D field-line chaos" indicates whether the simulation shows 3D dynamics with chaotic field lines.

threshold

$$L_{\rm th} \sim \pi b_g D \sim 0.1\pi b_g L_x, \tag{2}$$

given that approximately $D \sim 0.1L_x$. We will demonstrate this below with simulation Runs 1 and 2 in Table 1 with $b_g = 0.2$, $L_x \sim 150d_i$, so $L_{\rm th} \sim 9.5d_i$. They have L_y below and above $L_{\rm th}$ to be stable and unstable. As shown in Figure 1(a) with the current density, zooming onto two flux ropes, the flux ropes in Run 1 with $L_y = 6.25d_i < L_{\rm th}$ are stable to $m = 1$ kink, which are nearly 2D-like and laminar, although higher-harmonic ($m > 1$) kink modes may develop. In contrast, in Run 2, with twice the $L_y = 12.5d_i > L_{\rm th}$ and otherwise the same parameters (Figure 1(b)), the flux ropes present $m = 1$ flux rope kink instability, which tears up the otherwise closed flux surfaces and makes the reconnection layer turbulent with 3D field-line chaos.

This kink-driven field-line chaos facilitates 3D transport of the energetic particles out of the flux ropes. Figures 1(c) and (e) show the energetic electron and proton densities (with energy $1.2 < \varepsilon/m_i V_{\rm A}^2 < 2.4$) in the kink-stable simulation Run 1, while Figures 1(d) and (f) show those for the unstable simulation Run 2. The energetic particles for Run 1 are more constrained to the flux ropes, while those for Run 2 are more spread out in the layer. Note that the energetic ions in Run 1 in panel (e) appear less constrained than the electrons around the left flux rope, not because they leak out from the flux rope, but because there is a large exhaust to the right of this flux rope (also noticeable in panel (g) below), injecting some energetic ions locally into the presented energy range more efficiently than electrons. In fact, we find that these energetic ions only locally appear near the separatrix on one side ($z > 0$) of the exhaust (not shown), rather than leaking out to fill the volume. The asymmetry over z is likely because the parallel electric fields near the X-line accelerate the ions to bias toward one side of the exhaust.

3.2. Nonthermal Particle Acceleration

The particle transport out of the flux ropes enables the energetic particles to easily access the major Fermi acceleration regions at the reconnection exhausts for more efficient acceleration (Zhang et al. 2021). Figures 1(g)–(h) show $v_E \cdot \kappa$ in the x–z plane (v_E is the $E \times B$ drift velocity and κ is the magnetic curvature) that quantifies the field-line contraction and Fermi acceleration rate (Dahlin et al. 2017; Li et al. 2019b). Since the flux ropes being shown are propagating, there are both negative and positive values at two sides of the flux ropes that sum up to be zero, due to no net field-line contraction. But the field-line contraction at the exhausts outside the flux ropes has net positive acceleration rates. The transport out of the flux ropes allows particles to be efficiently accelerated in these exhaust regions.

Since the $m = 1$ kink instability controls the efficient acceleration, we take advantage of its L_y threshold $L_{\rm th}$ and perform a 3D simulation of unprecedented size in x with $L_x = 300d_i$ (Run 3 in Table 1). As a result, in this 3D simulation with $m = 1$ flux rope kink instability, both electrons and protons are accelerated into clear nonthermal power-law spectra (Figure 2), with indices around 4. The spectra have several distinct features: the low-energy bound of the power law (the shoulders $E_{l,e} \sim 0.2m_i V_{\rm A}^2$, $E_{l,i} \sim 0.5m_i V_{\rm A}^2$)) indicating the injection energy for particles, the power laws formed and extended by the Fermi acceleration process after injection, and the power-law high-energy cutoff ($E_{h,e} \sim E_{h,i} \sim 7m_i V_{\rm A}^2$) indicating the maximum energy particles are accelerated to.

The Fermi acceleration process can be described by a scaling analysis in Zhang et al. (2021). Using particle acceleration theory and considering Fermi acceleration at reconnection exhausts, we obtain

$$p \sim 1 + \frac{B_x}{B_z}\frac{\Delta_z}{L}\left(1 + \frac{B_g^2}{B_x^2}\right), \tag{3}$$

where Δ_z is the typical length scale in z of the exhaust field lines (related to the scale of the flux ropes), L is the half-length of the reconnecting current sheet, and the scales of the magnetic fields B_x and B_z are evaluated in the acceleration regions (exhausts). Considering Δ_z and L are both proportional to the domain size, they are roughly proportional to each other, and thus the predicted spectral indices remain unchanged for larger domains. According to the typical values in the exhausts in our low-guide-field simulations, we obtain $p \sim 4$, consistent with the simulation results as discussed in Zhang et al. (2021). Equation (3) not only applies to the low-guide-field regime, but also to the higher-guide-field regime, which will be further discussed below in Section 4.

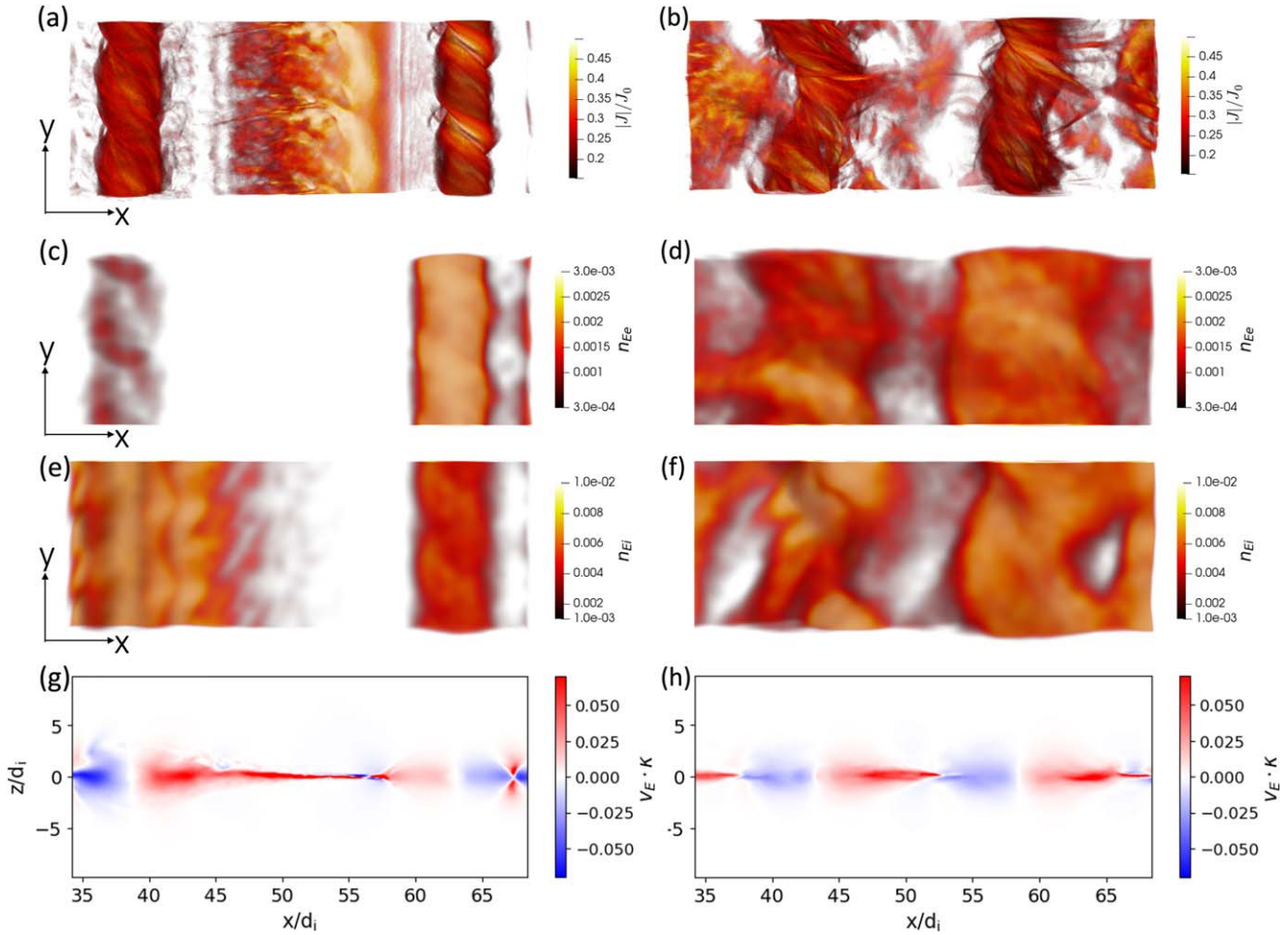

Figure 1. (a)–(b) show the current density $|J|/en_0c$ for Run 1 ($L_y = 6.25d_i$) and Run 2 ($L_y = 12.5d_i$), respectively, at $t\Omega_{ci} = 100$, zooming onto two flux ropes. (c)–(f) show the corresponding energetic electron and proton density (n_{Ee} and n_{Ei} with energy $1.2 < \varepsilon/m_i V_A^2 < 2.4$). The data for Run 1 have been duplicated in y using the periodic boundary to compare with Run 2. (g)–(h) show the corresponding $v_E \cdot \kappa$ averaged over y in the x–z plane, where v_E is the $E \times B$ flow and κ is the magnetic curvature vector, normalized to V_A and d_i.

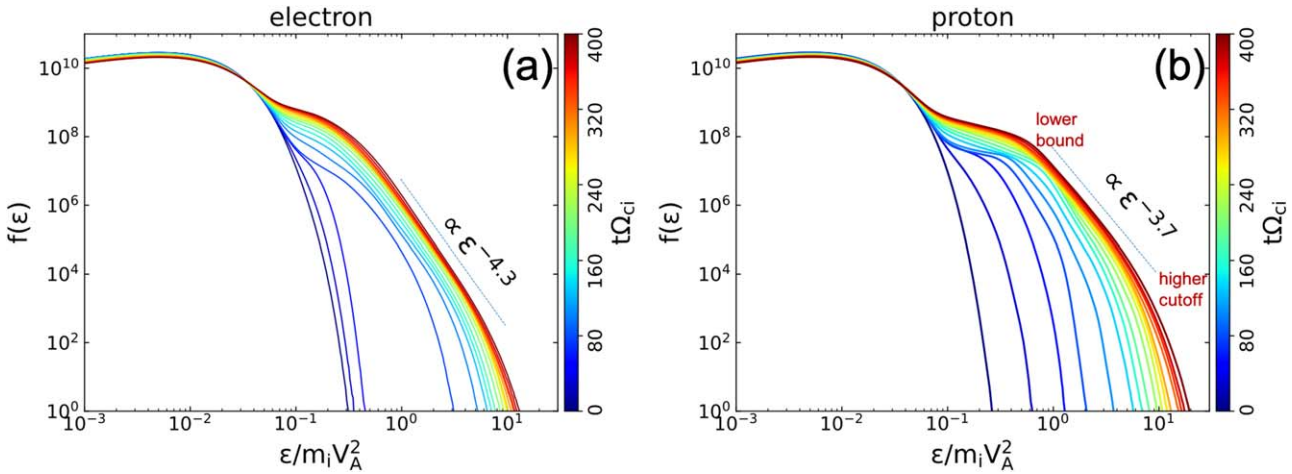

Figure 2. Evolution of energy spectra for electrons and protons in the large simulation Run 3.

3.3. Parameter Dependence

Here we examine the dependence of the energy spectra on parameters like plasma β (in the low-β regime) and the ion-to-electron mass ratio. Figures 3(a)–(b) show electron and proton spectra with two β in the low-β regime. Due to the temperature change, the upstream Maxwellian distribution has a significant shift, but the power-law slopes at higher energy remain very similar. Also, the low-energy shoulder of the proton spectrum remains essentially unchanged around $0.5m_i V_A^2$ (Zhang et al. 2021). This is because in the low-β regime, the magnetic tension and the Fermi reflection process are not sensitive to β, because the firehose instability does not set in until high β.

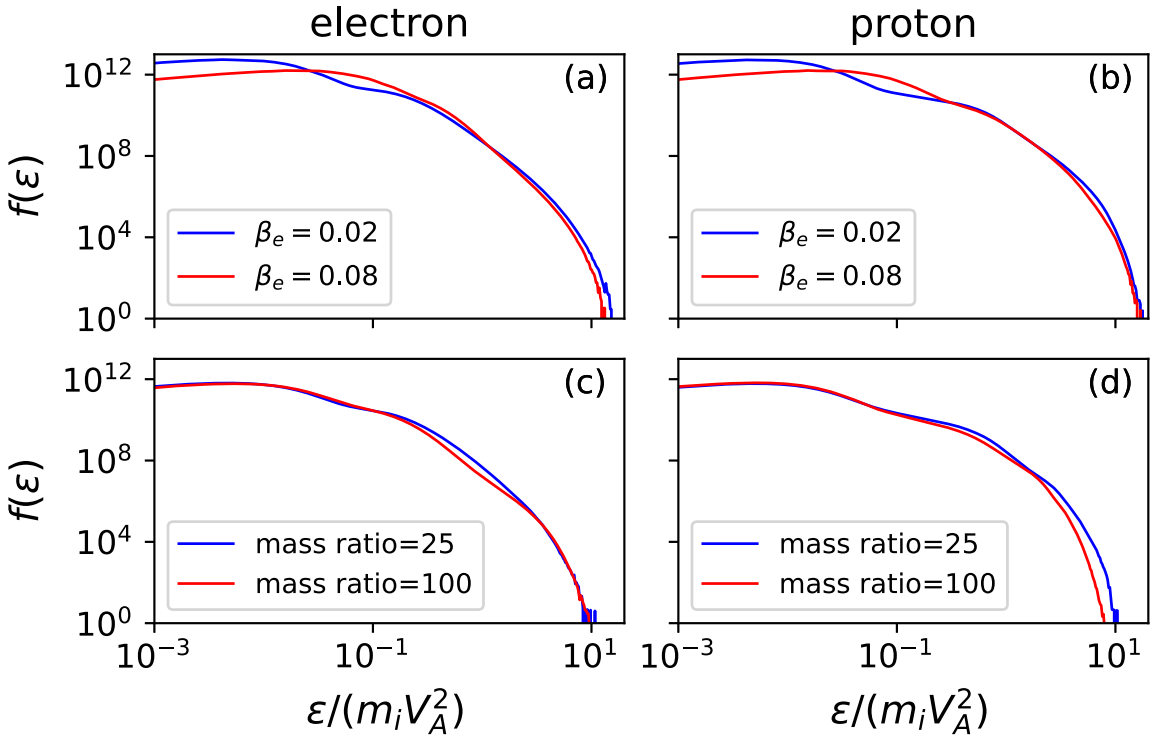

Figure 3. Dependence of energy spectra for electrons and protons. (a) and (b) show the dependence on β in Runs 2 and 4 at $t\Omega_{ci} = 200$. (c) and (d) show the dependence on mass ratio in Runs 5 and 6 at $t\Omega_{ci} = 125$.

Different β would not significantly affect the power-law slopes from the Fermi acceleration process and the low-energy shoulder of protons from the first Fermi reflection process (Zhang et al. 2021), which is consistent with our understanding of Fermi acceleration in reconnection. Figures 3(c)–(d) show weak dependence of the spectra on the mass ratio, although it is still far away from the realistic mass ratio. A higher mass ratio essentially reduces the electron mass in the simulation, so the ion acceleration may not substantially change with a higher mass ratio. Interestingly, the electron acceleration appears to have almost no change in the maximum energy with the mass ratio (panel (c)). The lack of extra electron acceleration for a higher mass ratio (smaller Larmor radii) suggests that the electrons are magnetized enough by magnetic flux ropes and exhausts to continue Fermi acceleration, even with mass ratio 25—notwithstanding that energetic electrons can be scattered and isotropized by 3D turbulence (Li et al. 2019b). Previous 2D simulations also showed no extra electron acceleration for higher mass ratios (Li et al. 2019a). In fact, the Larmor radii of energetic electrons for mass ratio 25 are still much less than the typical size of the flux ropes in simulations. As the particles get accelerated with $\varepsilon \propto t^{0.8}$ (Zhang et al. 2021), their Larmor radii ($\rho \propto \varepsilon^{0.5}$) grow much slower than the growth of the flux rope size ($\propto t$) as reconnection proceeds. Therefore, the energetic particles can actually get more and more magnetized by the flux ropes for further Fermi acceleration. This disagrees with a hypothesis in Arnold et al. (2021) that the energetic electrons in PIC simulations have too large Larmor radii and thus get demagnetized to stop Fermi acceleration, suppressing the extension of power laws. The more extended electron power laws in the macro-scale acceleration model (kglobal; Arnold et al. 2021) than PIC simulations may result from other important factors. They include the much larger effective domain sizes proportional to the acceleration time (Zhang et al. 2021, 2024), and the absence of pitch-angle scattering that maximizes the parallel energization favoring Fermi acceleration. This needs to be further explored.

3.4. Injection Process

Here, we explore the relative contribution of perpendicular and parallel electric fields during the particle injection process for both species using Run 3. Figure 4(a) shows the evolution of the total work done and its perpendicular-electric-field component, averaged within each different generation of electrons and protons starting acceleration at different times. Particles are included in a generation if the final energies are above the spectral low-energy bound and if the starting time of energization is within an $\Omega_{ci}\Delta t = 5$ interval. The figure shows that the protons are mostly injected by the perpendicular electric field, while the electrons are only half injected by it. We also show a histogram of the injection contribution percentage (Figure 4(b)), suggesting a similar conclusion: the proton perpendicular contribution peaks around 100%, while that of the electrons peaks around 50%.

We also show two representative particles (an electron and a proton) to demonstrate their injection process at reconnection exhausts. Figures 5(a)–(b) show the background of V_{ix} around the injection time of the particles, with the particle trajectories (colored by energy) overlaid. When the particles for the first time cross an exhaust from upstream, they get boosted to the injection energy (around $0.2m_i V_A^2$ for electrons and $0.5m_i V_A^2$ for protons), as shown in Figures 5(c)–(d). After injection, the particles wander elsewhere and get further Fermi acceleration.

3.5. Magnetic Power Spectra

The magnetic power spectra contain important information about the fluctuation energy in the reconnection layer, and they

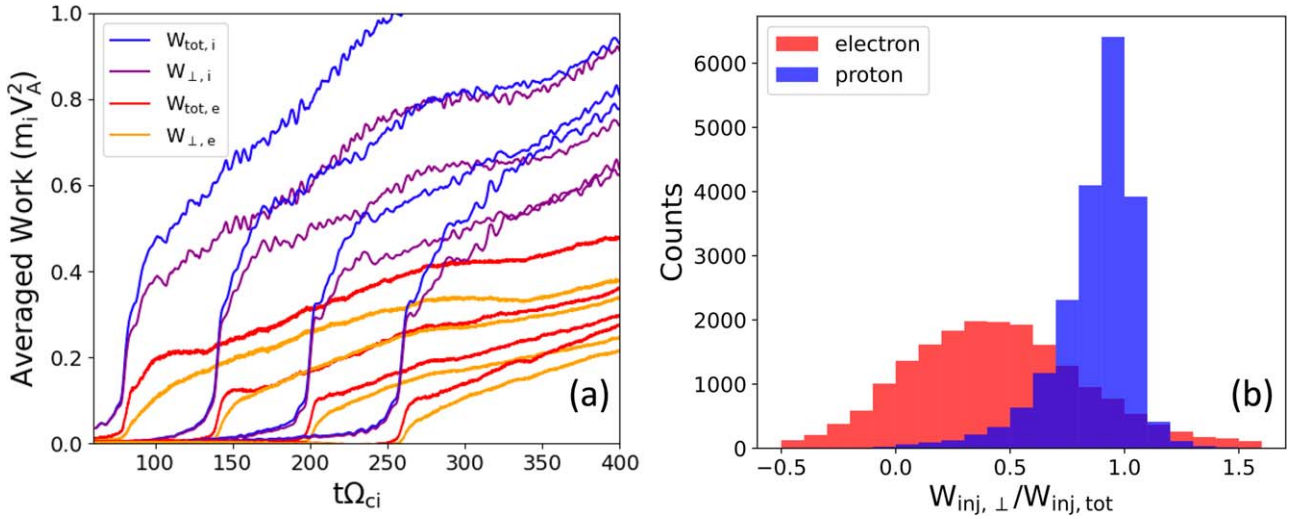

Figure 4. (a) Evolution of work done by the total and perpendicular component of electric fields for protons and electrons in Run 3, averaged over different generations of injected particles. (b) Histogram of the perpendicular work contribution fraction for injection for both species.

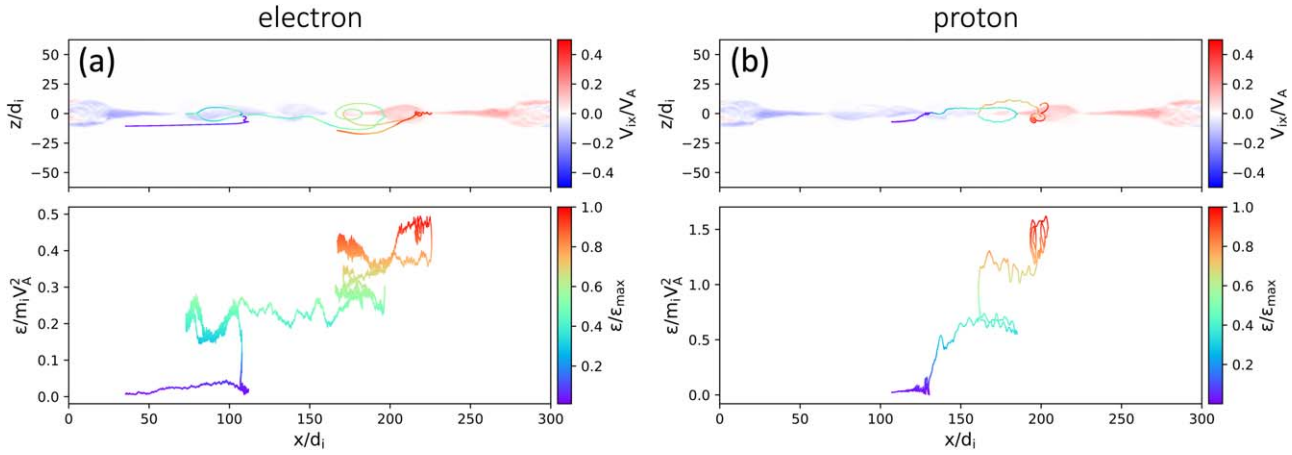

Figure 5. Representative particle trajectories in Run 3 demonstrating the injection process for both species, colored by the particle energy ε normalized by the maximum energy ε_{max}. The top panels show the proton velocity in x (V_{ix}) as backgrounds around the injection time of the particles (a 2D x–z slice at the y-location where the particle is injected).

are measured in both spacecraft observations and reconnection simulations. However, the magnetic power spectra do not appear to agree well between observations and simulations. Magnetospheric Multiscale (MMS) Mission observations along the turbulent reconnection layer at the magnetotail (Ergun et al. 2018, 2020) observe magnetic power spectra with indices $\alpha \sim 5/3$ and 3 below and above $kd_i \sim 1$. The observed frequent change of the B_z-direction indicates that it may be in the plasmoid reconnection regime relevant to our simulations. A recent paper (Richard et al. 2024) performed a statistical analysis over 24 reconnection jets and found an averaged power spectrum with similar indices as above, but with a shorter inertial range. Each individual event has a variety of power spectra (see their Figure 2(a)) and is harder to compare with. The $\alpha \sim 5/3$ index at super-ion scales is often suggested to be a signature of the inertial range of a Goldreich–Sridhar turbulence cascade, in which theory the vortex energy cascades across scales and forms spectra over $k_\perp$ with index $\alpha = 5/3$. Here, the $k_\perp$ describes perturbations perpendicular to a dominant uniform mean magnetic field. But reconnection at the magnetotail does not have a dominant uniform mean field, with significant field changes ($\Delta B/B \sim 1$) across the reconnection midplane and flux ropes. In fact, significant field changes within the inertial range scales are frequently observed in Ergun et al. (2018, 2020). Thus, reconnection does not have uniform parallel and perpendicular directions and it is not straightforward that the Goldreich–Sridhar cascade is applicable here. If we stick to this framework and average the fields over the whole reconnection region, the overall mean field is the guide field, and one can calculate $k_\perp$ spectra perpendicular to the guide field from simulations. Large-scale 3D fully kinetic simulations in the plasmoid reconnection regime have reconnection-driven 3D turbulence relevant to the observed turbulent reconnection (Daughton et al. 2014; Li et al. 2019b; Guo et al. 2021). In these simulations, the $k_\perp$ spectra have an index of about 2.7, which does not match the $5/3$ in observations. Therefore, it is not obvious that the $5/3$ index in observations corresponds to the Goldreich–Sridhar vortex cascade.

To better understand the spectra, we note that the MMS observations at the magnetotail probe the reconnection layer along the reconnection outflow direction, equivalently measuring spectra of k_x in the layer. To have a more reasonable comparison, we examine the region near the reconnection layer ($|z| < 15.6d_i$) to make spectra over k_x and average them over y

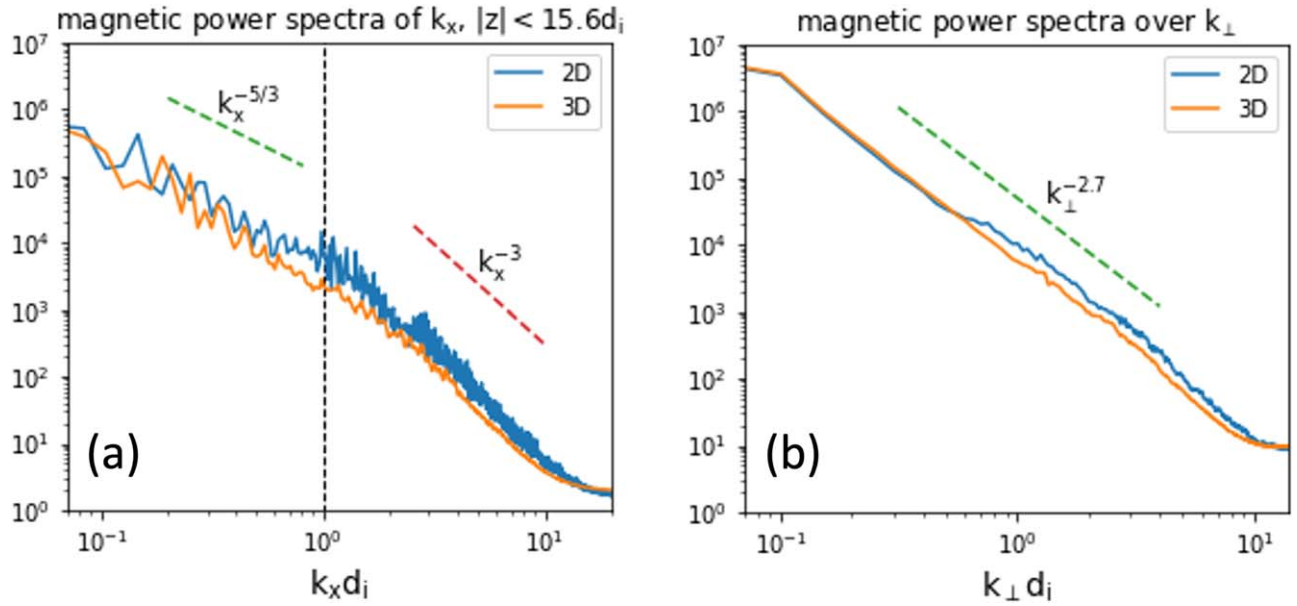

Figure 6. (a) Magnetic power spectra over k_x near the reconnection layer ($|z| < 15.6d_i$) for Run 3 at $t\Omega_{ci} = 200$ and for its 2D counterpart. Scalings $k_x^{-5/3}$ and k_x^{-3} are plotted for reference at low and high wavenumbers. (b) Magnetic power spectra over $k_\perp$ (perpendicular to the guide-field direction) for Run 3 at $t\Omega_{ci} = 200$ and for its 2D counterpart. A scaling $k_\perp^{-2.7}$ is plotted for reference. The 2D and 3D spectra are normalized to overlap and the vertical axes have arbitrary units.

and z from our simulation Run 3 in Figure 6(a). This spectrum demonstrates the power-law indices to be $\alpha \sim 5/3$ below $k_x d_i \sim 1$ and $\alpha \sim 3$ above it, in good agreement with the spectra measured by MMS (Ergun et al. 2018, 2020). Therefore, magnetic power spectra at the magnetotail can be naturally driven by reconnection. For comparison, we also show the $k_\perp$ spectrum following Li et al. (2019b) in Figure 6(b), which again produces a different $\alpha \sim 2.7$.

We also show the results for corresponding 2D simulations in Figures 6(a)–(b). Surprisingly, they are very similar to those for the 3D simulations, even though the 2D simulations have no 3D turbulence, with only laminar magnetic islands as the major magnetic structures. Therefore, the index $\alpha \sim 5/3$ in the k_x spectra does not necessarily indicate the Goldreich–Sridhar turbulence vortex cascade (Ergun et al. 2018, 2020), but likely corresponds to a reconnection-driven size distribution of magnetic flux ropes or islands. The $\alpha = 5/3$ spectra steepening at scales smaller than d_i is also consistent with the smallest flux ropes born in the kinetic reconnection current sheet. The largest scale in the $\alpha = 5/3$ spectra around $k_x d_i \sim 0.1$ also roughly corresponds to the largest flux rope width $\sim 60 d_i$ in x (see Figure 5). We also verify that in a smaller simulation, Run 2, the $\alpha = 5/3$ spectra have a shorter extension toward large scales (not shown), because of the smaller flux rope size (due to the shorter reconnection time). Interestingly, the higher-guide-field cases (those discussed in Section 4 below) have very similar k_x and $k_\perp$ spectral indices. We also verified that a longer L_y up to $0.5L_x$ ($L_x = 150d_i$, as in Li et al. 2019b) does not significantly change the spectral indices, regardless of the guide fields. We are preparing another upcoming paper that will quantitatively derive the island size distribution and the associated power spectra consistent with the observed spectra. For comparison, a previous study (Adhikari et al. 2020) used 2D reconnection simulations in the single X-line reconnection regime, and it found power spectra steepening over time, which can also have spectral indices close to $5/3$ during a phase of the simulation.

4. Reconnection with a Higher Guide Field

4.1. 3D Dynamics

In the higher-guide-field regime, we find in our simulations that the flux ropes from oblique tearing modes can keep growing over time as they are advected with the reconnection outflows. Meanwhile, the flux ropes still maintain their oblique angles, similar to the fastest-growing linear tearing mode, even during the interaction between two resonant layers. This is possibly because the oblique orientation of reconnection X-lines at the late stage is still controlled by a similar current filamentation tendency (Liu et al. 2015) and the X-line orientation guides the orientation of the flux ropes. Eventually, the flux ropes become large and proportional to the system size. These overlapping oblique flux ropes of large sizes control the full 3D field-line chaos in reconnection of higher guide fields. We demonstrate this in Figure 7 using simulations with $b_g = 0.6$, which can trigger oblique tearing modes and still have relatively strong Fermi acceleration compared to $b_g > 1$. To capture large oblique flux ropes in periodic domains of our simulations, the domain size in the guide-field direction L_y needs to be large enough. Below, we calculate the L_y threshold. Liu et al. (2013) predict the maximum oblique angle of tearing modes $\theta_c = \arctan(1/b_g)$ equal to the oblique angle of the upstream magnetic fields. Numerically, the fastest-growing mode occurs roughly around $\theta_m \sim \theta_c/1.5$. The growth rates for $\theta > \theta_m$ drop quickly, so θ_m is also approximately the maximum angle with significant growth rates to provide the 3D effects. Thus, we focus on capturing large oblique flux ropes with this angle $\theta = \theta_m$ in our 3D domains. Imagining such a flux rope with size D in the x-direction, from $y = 0$ to $y = L_y$, the cross section of this flux rope needs to displace in x for more than D, so that the flux rope does not "bite" its tail to violate the periodic boundary condition. So, the L_y threshold is

$$L_{\rm oblq} = D/\tan(\theta_m) \sim D/\tan(\theta_c/1.5) \sim 1.5D/\tan(\theta_c) = 1.5 b_g D. \quad (4)$$

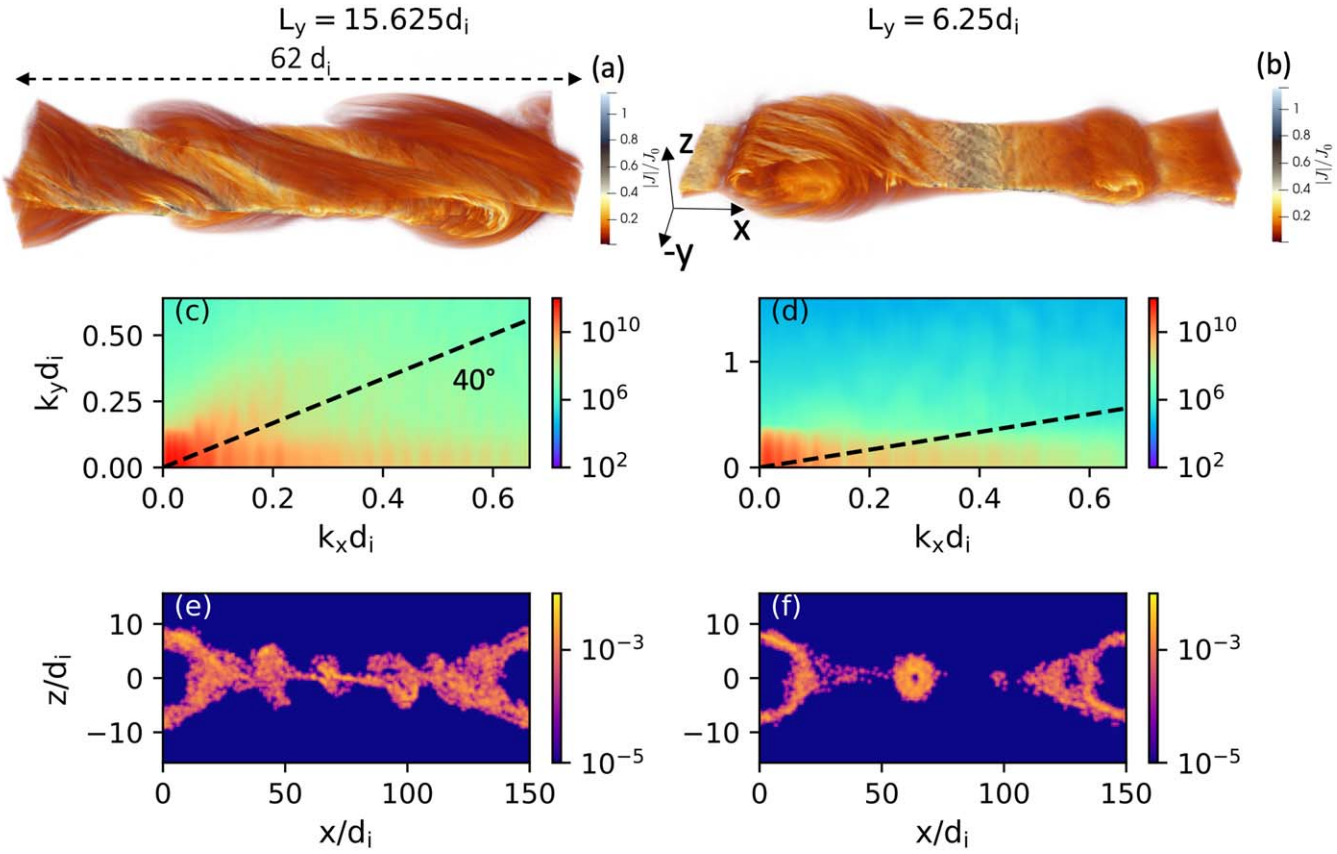

Figure 7. Current density $|J|/en_0c$ for simulations Run 7 and 8 with different y-dimensions (a) $L_y = 15.625d_i$ and (b) $L_y = 6.25d_i$, respectively, at $t\Omega_{ci} = 125$. The current density for Run 8 has been duplicated in y using the periodic boundary to compare with Run 7. Panels (c) and (d) show the corresponding Fourier analysis of B_z over k_x and k_y. An oblique angle of 40° from k_x is drawn with the dashed lines in both panels. Panels (e) and (f) show the corresponding energetic electron density ($1.2 < \varepsilon/m_i V_A^2 < 2.4$) at $y = 0$.

In the above simulation, $D \sim 10d_i$, $b_g = 0.6$, so $L_{\rm oblq} \sim 9d_i$ with $\theta_m \sim 40°$. We show a simulation above this threshold in Figure 7(a) and another one below in Figure 7(b). The above-threshold case presents clear bifurcating oblique flux ropes above and below the reconnection layer. The below-threshold case contains mostly only quasi-2D straight flux ropes. We show the corresponding Fourier analysis of B_z in Figures 7(c)–(d) in the space of k_x and k_y. A Blackman window is applied along z before the Fourier analysis to enforce a periodic boundary condition. The above-threshold case clearly has 3D oblique components with finite k_y, orienting at about $\theta_m = 40°$, which is consistent with the oblique angle of large oblique flux ropes estimated above. In contrast, the below-threshold case has only k_x, similar to a 2D simulation. We show the corresponding energetic electron density at $y = 0$ in Figures 7(e)–(f). The above-threshold case has energetic electrons spread throughout the reconnection layer, while the below-threshold case has them confined within the straight flux ropes.

4.2. Nonthermal Particle Acceleration

These 3D effects with field-line chaos (and particle spreading) for above-threshold cases can lead to more efficient acceleration. Figure 8 shows the increase in the energy spectrum flux ($f_{\rm 3D}/f_{\rm 2D}$) for electrons and protons in simulations with different L_y relative to the 2D counterpart, from below the threshold ($L_y = 6.25$) to highly above the threshold ($L_y = 75$). The below-threshold spectra are close to 2D ($f_{\rm 3D}/f_{\rm 2D} \sim 1$), while the above-threshold cases achieve more energetic particles at high energies. Due to the higher guide fields with weaker Fermi acceleration, the acceleration enhancement in 3D is weaker than the low-guide-field regime (Zhang et al. 2021). Interestingly, the $L_y = 15.62d_i$ case for electrons in cyan happens to have more acceleration than other above-threshold cases, but for ions it is only slightly more than the $L_y = 25$ case. We find in this run (Run 7) that there happen to be a couple of flux ropes stuck in the middle of the reconnection layer, without loss to the two large trapping islands at two ends, distinct from the other above-threshold runs. This can enable some energetic particles to stay around the middle of the reconnection layer for further acceleration without quick loss to two sides. This also facilitates the merging of these flux ropes that further accelerates energetic particles. In Figure 9, we show slices of B_z in the x–y plane at $z = 1.5d_i$ (on one side of the layer), in order to visualize the flux ropes merging to form a fairly big flux rope in the middle of the layer at $x \sim 70d_i$. Electrons have much higher speed than ions and likely more 3D transport along chaotic field lines to make full use of the additional acceleration. Since these stationary merging flux ropes only occur in this run likely by chance, we would not consider this L_y physically special among other runs.

We take advantage of this threshold in our domain size design to perform large 3D simulations of unprecedented size with $L_x = 300d_i$ (Runs 11 and 12 in Table 1). The upstream temperature is slightly higher than other simulations, so that the grid size can be slightly larger (maintaining the ratio to the Debye length), to make the computational costs feasible. With

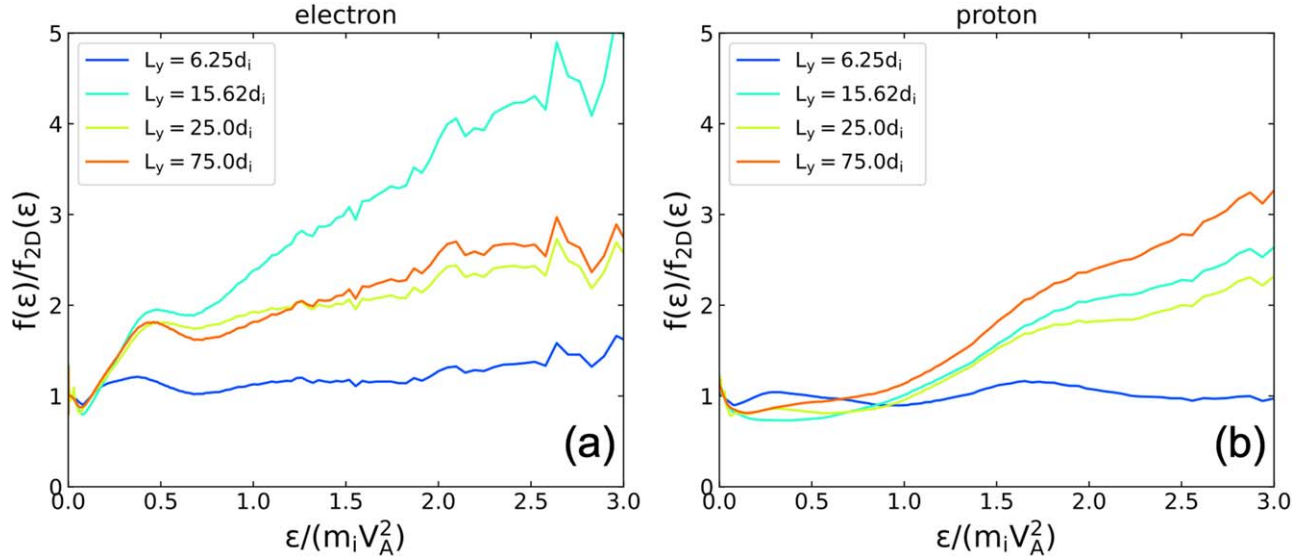

Figure 8. Energy spectra of both species relative to 2D for simulations with different L_y including Runs 7–10.

more efficient and continuous acceleration in 3D, our 3D simulations for the first time accelerate both species into nonthermal power-law spectra in the higher-guide-field regime. Figure 10 shows the spectra for guide field $b_g = 0.6$ in panels (a)–(b) and guide field $b_g = 1.0$ in panels (c)–(d). Here, the simulations run no more than 1 Alfvén crossing time (in contrast to 1.3 for low guide fields), because we find that higher guide fields hinder the compression of the two large islands at the two ends of the reconnection layer, which enlarge their sizes to press back onto the reconnection layer at earlier times than for low guide fields—as an artifact of the periodic boundary in x. We apply Equation (3) from Fermi acceleration to the higher guide fields here by only changing $B_g/B_x \sim b_g$. While it predicts $p \sim 4$ for low guide fields, it predicts $p \sim 5$ for $b_g = 0.6$ and $p \sim 7$ for $b_g = 1$. Figure 10 shows electron and proton spectra reaching $p \sim 5$ for $b_g = 0.6$ and $p \sim 6.5$ for $b_g = 1$, roughly consistent with the prediction above from Fermi acceleration. The steeper spectra for higher guide fields result from the weaker Fermi acceleration. Note that near the end of the simulations, the high-energy portions of the ion power-law spectra continue to extend to higher energy, but the shoulders from injection shift to somewhat lower energies, due to the reduction of the upstream magnetic flux and thus $m_iV_A^2$ (getting 1.3 times lower). This leads to a slight distortion of the ion power-law spectra around the shoulders near the end of the simulations. However, this is just a limitation of the periodic boundaries over z and it would not occur in reality with open incoming upstream flux.

4.3. Oblique Flux Rope Kink Instability

We discover that the overlapping oblique flux ropes are not the only important process of the 3D dynamics with higher guide fields. The oblique flux ropes will experience the $m = 1$ kink instability when L_y exceeds a new threshold $L_{\rm kink}$. For example, Figures 11(a)–(b) show two above-$L_{\rm oblq}$ simulations of $b_g = 0.6$, below and above $L_{\rm kink} \sim 50d_i$ (to be calculated below), with $L_y = 25$ and $75d_i$, respectively. The oblique flux ropes are formed and the reconnection bidirectional outflows in x pull each flux rope to both sides, resulting in some thinner elongated structures around the middle of the x-direction. With $L_y = 25d_i$, 3D oblique flux ropes can exist, but they are straight (indicated by the black line) and do not show extra $m = 1$ kink dynamics. With $L_y = 75d_i$, the oblique flux ropes are long enough to be $m = 1$ kink-unstable, driving extra exotic 3D kinking dynamics. We calculate $L_{\rm kink}$ in the following. As demonstrated in Figure 12, consider an oblique flux rope with the angle θ_m and width D in x. The cross section perpendicular to this oblique flux rope has a diameter $D\cos(\theta_m)$. The angle between the upstream magnetic field $\boldsymbol{B}_{\rm upstream}$ and the flux rope is $\theta_c - \theta_m \sim 0.5\theta_m$. Since the upstream fields eventually wrap around the edge of the flux rope to become $\boldsymbol{B}_{\rm edge}$, we can use the direction of the upstream field to calculate the minimum length of the flux rope to be $m = 1$ kink-unstable as $L_{\rm FR} = \pi D\cos(\theta_m)/\tan(0.5\theta_m)$ (for the field to wrap around one circle). To contain this flux rope with periodic boundaries, a simulation needs to have a minimum L_y:

$$L_{\rm kink} = L_{\rm FR} * \cos(\theta_m) = \pi D\cos^2(\theta_m)/\tan(0.5\theta_m). \quad (5)$$

For $D = 10d_i$ (from the simulation), $b_g = 0.6$, we get $L_{\rm kink} \sim 50d_i$. This puts $L_y = 75d_i$ above the threshold and $L_y = 25d_i$ below the threshold, consistent with the simulations. Such oblique flux rope kink instability drives extra 3D turbulent dynamics into the reconnection layer, which could potentially fragmentize the oblique flux ropes in a sufficiently large domain to turn the layer into a fully turbulent state—filled with fragmented kinking oblique flux ropes growing over time. An important question is whether this extra 3D turbulent dynamics can lead to extra acceleration. In Figure 8, the $L_y = 75d_i$ case shows some enhanced acceleration from the $L_y = 25d_i$ case, but it is not substantial, with the enhancement of protons somewhat more than electrons. This is possibly because the overlapping oblique flux ropes with $L_y = 25d_i$ already have sufficient field-line chaos for efficient acceleration, especially for the electrons with high speed. The effects of this extra instability will be further explored, likely with larger-scale hybrid simulations with particle ions and fluid electrons (Zhang et al. 2024).

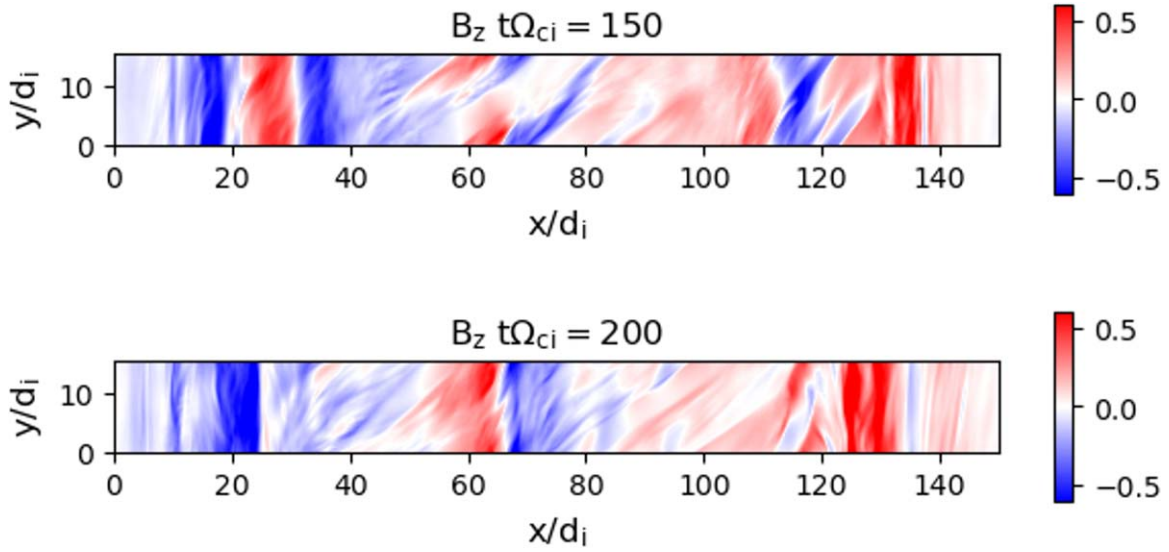

Figure 9. Slices of B_z in the x–y plane at $z = 1.5d_i$ at different times of Run 7 to illustrate the stationary flux ropes merging to form a bigger flux rope in the middle of the layer.

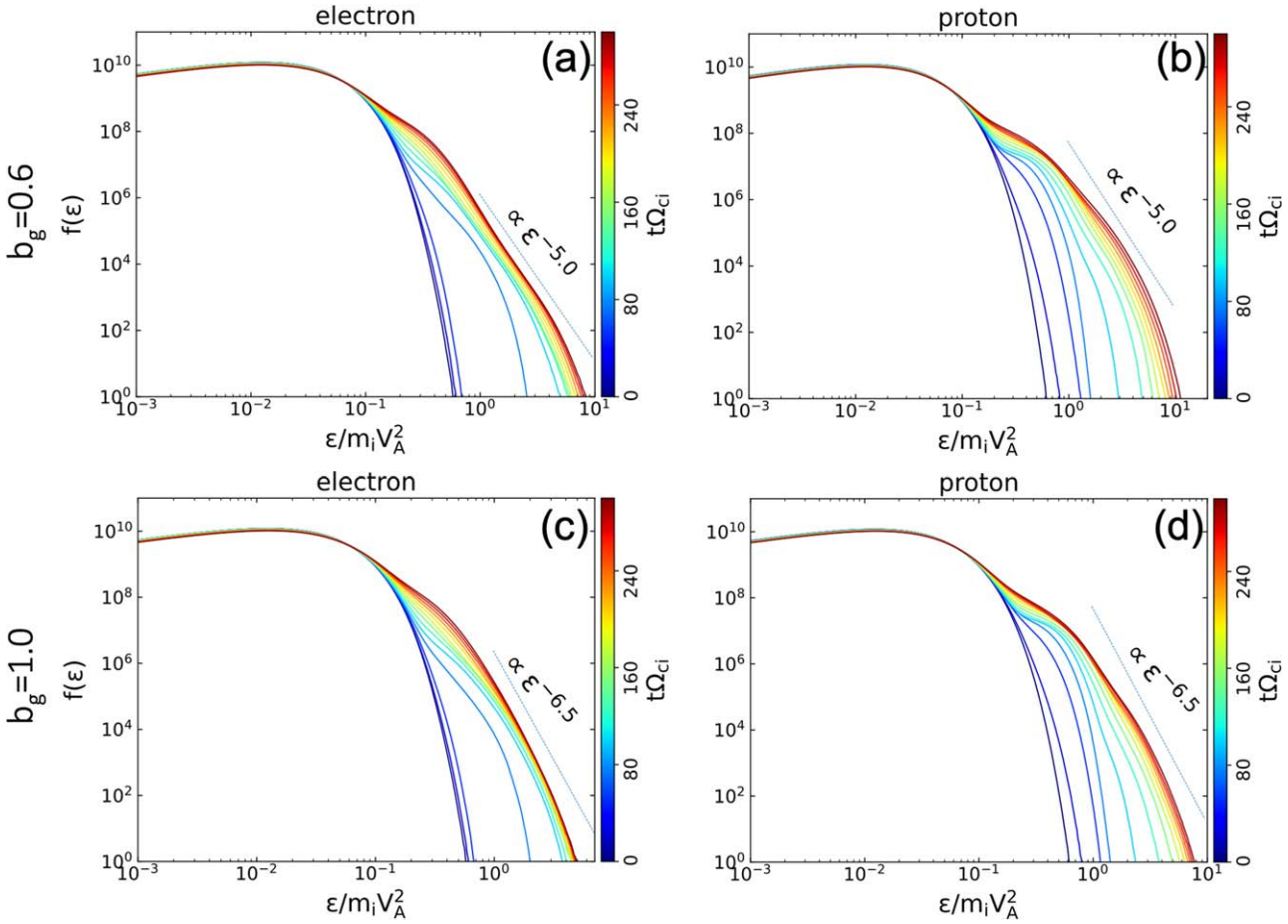

Figure 10. Evolution of energy spectra for electrons and protons in the large simulations of Runs 11 and 12, with guide fields of 0.6 and 1, respectively.

5. Observation Implications

The magnetic power spectra, 3D flux rope dynamics, and energetic particle spectra in our simulations should have implications for remote sensing and in situ satellite observations of 3D reconnection. The magnetic power spectra insensitive to guide-field and 3D effects suggest a common power spectral index $\alpha \sim 5/3$ (reflecting a common island size distribution) measured along outflow directions for different

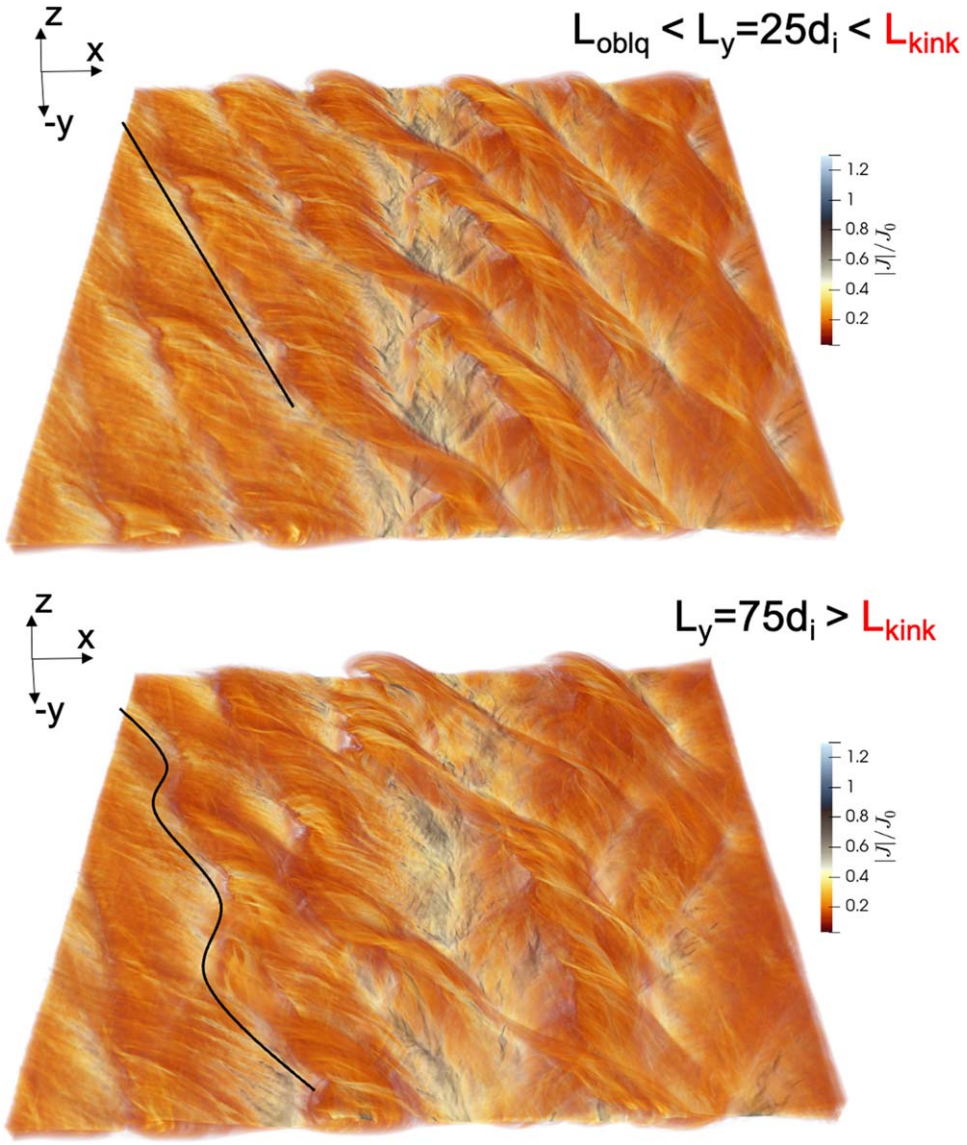

Figure 11. Current density $|J|/en_0c$ for simulation Runs 9 and 10 with different L_{ys}, around $t\Omega_{ci} = 80$. The relations to the L_y thresholds $L_{\rm oblq}$ (for large oblique flux ropes) and $L_{\rm kink}$ (for oblique kink instability) are indicated. The two black lines near the flux rope edges emphasize their straight and kinking shapes.

reconnection-driven phenomena, such as at the magnetotail, the magnetopause, the heliospheric current sheet, and solar flares. The 3D kink dynamics of the flux ropes suggest the local orientations of various flux ropes would swing in in situ measurements. Specially with a guide field, the local orientation of the flux ropes at the two sides of the reconnection midplane bifurcates to two distinct directions, with additional kinking swing around each direction. The downstream particle energy spectra should consist of a shoulder from injection and a power law from acceleration. The energy of the shoulder for ions $\sim m_i V_{\rm A}^2$ is somewhat higher than that for electrons. The considerable guide-field dependence of the power-law spectral indices (Equation (3)) can partly explain the wide range of observed indices (Oka et al. 2018; Omodei et al. 2018; Bale et al. 2023). The hardest spectral indices $p \sim 4$ should be produced by low-guide-field, low-β reconnection, such as in the magnetotail (Ergun et al. 2020), the heliospheric current sheet (Desai et al. 2022), and the impulsive phase of solar flares (Chen et al. 2020); reconnection with higher guide fields is expected to have softer indices.

6. Conclusion

It has been a long-standing effort to understand the physics of nonthermal particle acceleration in 3D magnetic reconnection, which shows contrasting dynamics for different guide fields. In this paper, we have explored this by performing fully kinetic simulations with various parameters and domain sizes in both the weak- and stronger-guide-field regimes. In both regimes, we have uncovered the distinct 3D dynamics that lead to field-line chaos and efficient acceleration in reconnection, and we have achieved nonthermal acceleration into power-law spectra. In the low-guide-field regime, the flux rope kink instability enables the 3D dynamics for efficient acceleration. We took advantage of the flux rope kink instability threshold to optimize our simulation domains to achieve the power-law spectra. The weak dependence of the spectra on the ion-to-

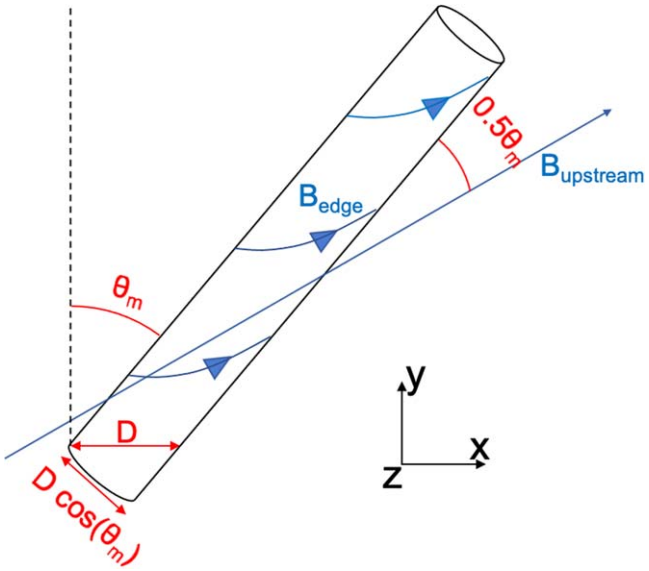

Figure 12. A schematic picture that demonstrates the upstream magnetic fields wrapping around the edge of the oblique flux rope, in order to estimate the L_y threshold $L_{\rm kink}$ for the oblique kink instability.

electron mass ratio and β ($\ll$1) implies that the plasma is magnetized enough by the magnetic flux ropes and adjacent exhausts for Fermi acceleration in our PIC simulations. While both electrons and protons are injected at reconnection exhausts, protons are primarily injected by perpendicular electric fields through Fermi reflections and electrons are injected by a combination of perpendicular and parallel electric fields. The magnetic power spectra suggest that reconnection can naturally drive the magnetic power spectra measured in the in situ magnetotail observations. The power spectra may not indicate the Goldreich–Sridhar turbulence vortex cascade, but may instead reflect the size distribution of magnetic islands/flux ropes. In the higher-guide-field regime, the oblique flux ropes of large sizes control the domain size threshold to capture the major 3D dynamics for efficient acceleration. We have also made use of the threshold in designing domain sizes to achieve nonthermal acceleration into power laws in energy spectra, with indices consistent with the prediction of Fermi acceleration dependent on guide fields. Intriguingly, the oblique flux ropes can also experience flux rope kink instability, driving extra exotic 3D dynamics for the reconnection layer that could potentially fragmentize the oblique flux ropes—although it has not substantially further enhanced the acceleration. The effect of this instability on the 3D dynamics and particle acceleration will be further explored.

This study also has some limitations. While our large-scale fully kinetic simulations have domain sizes ($L_x \sim 300d_i$) comparable to magnetospheric reconnection layers, they are still much smaller than macroscopic astrophysical systems, such as solar flares. However, the continuous Fermi acceleration and power-law extension (shown in this paper and Zhang et al. 2021) suggest that the power laws can continue to extend to much higher energy in macroscopic systems. The mass ratios in 3D simulations explored in this paper, though with a weak dependence, are still far from the realistic ratio due to the computational cost constraints, which may be further investigated in the future.

This work has broad implications for particle acceleration by 3D magnetic reconnection with a variety of guide fields, in not only heliosphysics (such as reconnection in the magnetosphere, solar winds, and the solar corona), but also astrophysics (such as stellar flares and accretion disk flares; Nathanail et al. 2020; Ripperda et al. 2020).

Acknowledgments

We gratefully acknowledge the helpful discussions in the SolFER DRIVE Science Center collaboration. Q.Z., F.G., W.D., and H.L. acknowledge the support from Los Alamos National Laboratory through the LDRD program and its Center for Space and Earth Science (CSES), DOE OFES, and NASA programs through grants NNH17AE68I, 80HQTR20T0073, 80NSSC20K0627, 80HQTR21T0103, and 80HQTR21T0005, and through the Astrophysical Theory Program. The simulations used resources provided by the Los Alamos National Laboratory Institutional Computing Program, the National Energy Research Scientific Computing Center (NERSC), and the Texas Advanced Computing Center (TACC).

ORCID iDs

Qile Zhang https://orcid.org/0000-0002-9504-641X
Fan Guo https://orcid.org/0000-0003-4315-3755
William Daughton https://orcid.org/0000-0003-1051-7559
Xiaocan Li https://orcid.org/0000-0001-5278-8029
Hui Li https://orcid.org/0000-0003-3556-6568

References

Adhikari, S., Shay, M. A., Parashar, T. N., et al. 2020, PhPl, 27, 042305
Arnold, H., Drake, J. F., Swisdak, M., et al. 2021, PhRvL, 126, 135101
Bale, S. D., Drake, J. F., McManus, M. D., et al. 2023, Natur, 618, 252
Bowers, K., & Li, H. 2007, PhRvL, 98, 035002
Bowers, K. J., Albright, B. J., Yin, L., Bergen, B., & Kwan, T. J. T. 2008, PhPl, 15, 055703
Chen, B., Shen, C., Gary, D. E., et al. 2020, NatAs, 4, 1140
Cheng, X., Li, Y., Wan, L. F., et al. 2018, ApJ, 866, 64
Cohen, C. M. S., Christian, E. R., Cummings, A. C., et al. 2020, A&A, 650, A23
Dahlburg, R. B., Antiochos, S. K., & Zang, T. A. 1992, PhFlB, 4, 3902
Dahlin, J. T., Drake, J. F., & Swisdak, M. 2014, PhPl, 21, 092304
Dahlin, J. T., Drake, J. F., & Swisdak, M. 2016, PhPl, 23, 120704
Dahlin, J. T., Drake, J. F., & Swisdak, M. 2017, PhPl, 24, 92110
Daughton, W. 1998, JGR, 103, 29429
Daughton, W., Nakamura, T. K. M., Karimabadi, H., Roytershteyn, V., & Loring, B. 2014, PhPl, 21, 052307
Daughton, W., Roytershteyn, V., Karimabadi, H., et al. 2011, NatPh, 7, 539
Desai, M. I., Mitchell, D. G., McComas, D. J., et al. 2022, ApJ, 927, 62
Drake, J. F., Swisdak, M., Che, H., & Shay, M. A. 2006, Natur, 443, 553
Ergun, R. E., Ahmadi, N., Kromyda, L., et al. 2020, ApJ, 898, 154
Ergun, R. E., Goodrich, K. A., Wilder, F. D., et al. 2018, GeoRL, 45, 3338
French, R. J., Judge, P. G., Matthews, S. A., & van Driel-Gesztelyi, L. 2019, ApJL, 887, L34
Gary, D. E., Chen, B., Dennis, B. R., et al. 2018, ApJ, 863, 83
Guo, F., Li, H., Daughton, W., & Liu, Y.-H. 2014, PhRvL, 113, 155005
Guo, F., Li, X., Daughton, W., et al. 2021, ApJ, 919, 111
Guo, F., Liu, Y.-H., Li, X., et al. 2020, PhPl, 27, 080501
Haggerty, C. C., Shay, M. A., Drake, J. F., Phan, T. D., & McHugh, C. T. 2015, GeoRL, 42, 9657
Johnson, G., Kilian, P., Guo, F., & Li, X. 2022, ApJ, 933, 73
Krucker, S., Hudson, H. S., Glesener, L., et al. 2010, ApJ, 714, 1108
Le, A., Egedal, J., Daughton, W., Fox, W., & Katz, N. 2009, PhRvL, 102, 085001
Li, X., Guo, F., & Li, H. 2019a, ApJ, 879, 5
Li, X., Guo, F., Li, H., & Birn, J. 2018, ApJ, 855, 80
Li, X., Guo, F., Li, H., & Li, G. 2017, ApJ, 843, 21
Li, X., Guo, F., Li, H., Stanier, A., & Kilian, P. 2019b, ApJ, 884, 118
Li, X., Guo, F., & Liu, Y.-H. 2021, PhPl, 28, 052905
Lin, R. P. 2011, SSRv, 159, 421
Liu, W., Li, H., Yin, L., et al. 2011, PhPl, 18, 052105

Liu, Y.-H., Daughton, W., Karimabadi, H., Li, H., & Roytershteyn, V. 2013, PhRvL, 110, 265004
Liu, Y.-H., Hesse, M., & Kuznetsova, M. 2015, JGRA, 120, 7331
Nathanail, A., Fromm, C. M., Porth, O., et al. 2020, MNRAS, 495, 1549
Oka, M., Birn, J., Battaglia, M., et al. 2018, SSRv, 214, 82
Oka, M., Birn, J., Egedal, J., et al. 2023, SSRv, 219, 75
Oka, M., Krucker, S., Hudson, H. S., & Saint-Hilaire, P. 2015, ApJ, 799, 129
Omodei, N., Pesce-Rollins, M., Longo, F., Allafort, A., & Krucker, S. 2018, ApJL, 865, L7
Onofri, M., Isliker, H., & Vlahos, L. 2006, PhRvL, 96, 151102
Oz, E., Myers, C. E., Yamada, M., et al. 2011, PhPl, 18, 102107
Richard, L., Sorriso-Valvo, L., Yordanova, E., Graham, D. B., & Khotyaintsev, Y. V. 2024, PhRvL, 132, 105201
Ripperda, B., Bacchini, F., & Philippov, A. A. 2020, ApJ, 900, 100
Shih, A. Y., Lin, R. P., & Smith, D. M. 2009, ApJL, 698, L152
Yamada, M., Kulsrud, R., & Ji, H. 2010, RvMP, 82, 603
Zenitani, S., & Hoshino, M. 2005, ApJL, 618, L111
Zhang, Q., Drake, J. F., & Swisdak, M. 2019a, PhPl, 26, 072115
Zhang, Q., Drake, J. F., & Swisdak, M. 2019b, PhPl, 26, 102115
Zhang, Q., Guo, F., Daughton, W., Li, H., & Li, X. 2021, PhRvL, 127, 185101
Zhang, Q., Guo, F., Daughton, W., et al. 2024, PhRvL, 132, 115201